



OPEN

Sex-based differences in cell migration on aligned topographies

Yang Hu^{1,7}, Yin Mei Chan^{2,7}, Nicola G. Judge², Matthew L. Becker^{2,3,4,5} & Rebecca K. Willits^{1,6}✉

Sexual dimorphism has been observed in many physiological and pathological responses, yet few studies incorporate both female and male experimental groups for preclinical work. For the development of biomaterial devices, *in vitro* studies are essential for design and optimization, and quantitative comparison of female and male cell migratory behavior is a crucial design consideration. In this work, we thoroughly examined sex-based migration on flat controls and aligned nanofiber scaffolds of various diameters using anomalous and random walk models. Male and female cells exhibited significantly different migration on flat substrates, with female cells having increased speed while male cells had higher persistence. Persistence increased with the introduction of aligned fiber topography for female cells, but only affected male cells on the highest fiber diameter. Speed along the axis of alignment differed between sexes on 1.2 and 1.8 μm fibers. Morphological analysis confirmed cell shape was a function of both sex and fiber size. These results provided critical information regarding sex-based cell migration, highlighting the importance of sex within *in vitro* studies for clinical device design.

Keywords Schwann cells, Sex-based differences, Cell migration, Nanofibers

Sex-based differences at the biochemical and cellular levels have been widely recognized in several species^{1–4}. Sex-dependent behaviors in both physiological and pathological responses, including immune response, drug efficacy, wound healing, neurodegeneration, and gene expression have also been documented^{5–8}. Despite widespread knowledge of these differences, only ~10% of publications in tissue engineering and regenerative medicine in 2019 reported the use of both female and male subjects, obscuring biological behaviors that would advance understanding and expedite new biomaterial development and device innovation⁹. Specifically for the nervous system, clinical studies have corroborated sex-based differences in nervous system injuries such as stroke, traumatic brain injury, and brain disorganization^{10–12}. Such sex-based differences in peripheral nerve injury and regeneration have been largely derived from *in vivo* animal studies^{13–15}, with most studies focused on hormonal regulation or genetic differences following nerve injury¹⁶. These studies highlight that sex-based differences are likely discoverable *in vitro*, and thus, examination of these differences within early preclinical studies should be considered during the design and development of new devices.

The current state-of-the-art clinical repair technique for critical-size nerve gap injuries (~3–4 cm in humans) is the autologous graft^{17,18}. However, this technique leads to donor site morbidity and the recovery of motor function occurs in less than 40% of cases^{19,20}. As such, new devices to support regeneration after large transection injuries have emerged at the forefront of translational research efforts. FDA-approved single lumen conduits have been insufficient to address long-gap injuries, and therefore, various fillers, including collagen and collagen/glycosaminoglycan, are currently being used to increase the regenerative capacity of off-the-shelf designs²¹. Biodegradable synthetic polymers that encourage cell infiltration are particularly attractive for their ability to provide architectural support and scalable, translationally relevant manufacturing strategies without eliciting long-term immunological concerns²².

Preclinical studies for new synthetic materials for nerve regeneration have focused on axonal elongation²³, as well as Schwann cell proliferation²⁴ and migration²⁵ *in vitro*. Although many external stimuli can influence cell migration and infiltration, substrate topography is a key element in the design of new devices and technology^{23,25}. Nanofibers offer high surface-area-to-volume ratios that promote cell attachment and provide topological cues to enhance guidance and directionality of regenerating nerves²⁶. Cavanaugh et al. previously showed that aligned,

¹Department of Chemical Engineering, Northeastern University, Boston, MA 02115, USA. ²Department of Chemistry, Duke University, Durham, NC 27708, USA. ³Department of Mechanical Engineering and Materials Sciences, Thomas Lord, Duke University, Durham, NC 27708, USA. ⁴Department of Biomedical Engineering, Duke University, Durham, NC 27708, USA. ⁵Department of Orthopedic Surgery, Duke University, Durham, NC 27708, USA. ⁶Department of Bioengineering, Northeastern University, Boston, MA 02115, USA. ⁷Yang Hu and Yin Mei Chan have contributed equally. ✉email: matthew.l.becker@duke.edu; r.willits@northeastern.edu

touch-spun polycaprolactone (PCL) nanofibers directionally influenced individual Schwann cell migration by exploitation of contact guidance, limiting the direction of migration to the axis of fiber alignment²⁵. However, only female rat cells and explants were studied.

In this study, migratory responses of both female and male Schwann cells on aligned touch-spun allyl-functionalized poly(ϵ -caprolactone) (allyl-PCL) nanofibers were quantified. Female Schwann cells exhibited greater speeds and male cells had higher persistence on laminin-coated control substrates, revealing inherent sex-based differences. Cell morphologies, speeds, and migratory patterns further indicated response to fiber topographies was both sex and diameter dependent. These results reveal critical information regarding Schwann cell response to topography, promoting clinical nerve regenerative practices in both female and male hosts.

Materials

All materials used in this study are provided in the SI (see SI materials).

Methods

Polymerization and NMR characterization of allyl-functionalized poly(ϵ -caprolactone) (allyl-PCL)

Mg(BHT)₂(THF)₂ and 6-allyl- ϵ -caprolactone were synthesized as described previously (Figs S1, S3 and S4)^{27,28}. In a glovebox (H₂O < 0.1 ppm, O₂ < 0.1 ppm), a solution of Mg(BHT)₂(THF)₂ (catalyst, 2.96 g, 4.86 mmol) and isopropanol (initiator, 0.97 mmol, 0.002 eq.) was dissolved in dry toluene (8 mL). This mixture was subsequently added to ϵ -caprolactone (41.63 g, 36.48 mmol) and 6-allyl- ϵ -caprolactone (18.75 g, 12.16 mmol) in dry toluene (350 mL) (Fig. S2). The vessel was sealed, removed from the glovebox, and left to stir for 5 h at 60 °C. The reaction was then quenched with trifluoroacetic acid (TFA) and the polymer was thrice precipitated into cold *n*-hexanes. The resulting polymer was dried *in vacuo* overnight, collected as a yellow/white solid, and analyzed via ¹H NMR (500 MHz, CDCl₃): δ = 5.87–5.80 (m, 1H, CH=CH₂), 5.14–5.01 (m, 2H, CH=CH₂), 4.3–4.22 (m, 1H, CH-O), 2.69–2.56 (m, 2H, CH₂-CO), 2.50–2.29 (m, 2H, CH₂-CH=), 1.96–1.90 (m, 2H, CH₂-CH), 1.62–1.53 (m, 2H, CH₂) ppm (Fig. S5). Proton (¹H) nuclear magnetic resonance (NMR) spectroscopy and ¹³C NMR spectroscopy were performed in CDCl₃ on a Bruker Advance NEO at 500 MHz (23 °C) with a 5 mm iProbe.

Thermal (TGA and DSC) and molecular properties (SEC) characterization of allyl-functionalized poly(ϵ -caprolactone) (allyl-PCL)

Thermogravimetric analysis (TGA) was performed on a TA Instruments Discovery TGA 550 (TA Instruments–Waters L.L.C, New Castle, DE). Samples of 5–10 mg were loaded onto a platinum TGA pan and equilibrated at room temperature. The samples were heated to 120 °C at a ramp rate of 10 °C/min, held isothermally for 10 min, and finally heated to 800 °C at 10 °C/min. The degradation temperature (*T_d*) was determined as the temperature at 5% mass loss. Differential scanning calorimetry (DSC) analysis was performed on a TA Instruments Discovery DSC 250. Samples of approximately 5 mg were loaded onto a hermetic aluminum DSC pan. The temperature range scanned was –80–200 °C at a heating rate of 10 °C/min and a cooling rate of 5 °C/min. The crystallization temperature (*T_c*) was calculated as the peak height in the first cooling scan. To eliminate thermal history, the melt transition temperature (*T_m*) was determined as the peak temperature and the glass transition temperature (*T_g*) was determined as the midpoint of the transition in the second heating cycle. TGA and DSC plots are shown in Figs. S7 and S8: *T_{d,5%}* = 265 °C, *T_g* = –59 °C, *T_c* = –4 °C, *T_m* = 37.5 °C. Size exclusion chromatography (SEC) analysis was performed on an EcoSEC HLC-8320GPC (Tosoh Bioscience LLC, King of Prussia, PA) with a TSKgel GMHHR-M mixed bed column, refractive index (RI) detector and poly(styrene) standards. Samples (2.5 mg/mL) were prepared with HPLC-grade chloroform (amylene-stabilized) for injection with a 0.5 mL/min flow rate at 40 °C to determine molecular mass (*M_n* and *M_w*), and molecular mass distribution (*D_M*). The SEC chromatogram is shown in Fig. S6: *M_n* = 81.6 kDa, *M_w* = 114 kDa, *D_M* = 1.40 (SEC CHCl₃, based on PS standards).

Fabrication and diameter characterization of touch-spun aligned nanofibers

Allyl-PCL was dissolved in chloroform (25 w/w%) and the polymer solution was drawn into a glass syringe (1 mL), fixed to a blunt-end needle (18G), and loaded onto a syringe pump. Polymer was dispensed out of the syringe at a constant flow rate (5 μ L/min) for all touch-spun substrates. Borosilicate coverslips were used as the collection plates. The syringe pump was positioned so that the tip of the needle was in tangential contact with the rotating, perpendicular rods connected to the rotating disk. An illustration of the touch-spinning setup is shown in Fig. 1A–D. The speed of the rotating disk was varied to yield different fiber diameters. Sputter coating was done using a Denton Desk V Sputter-Coater with gold at a coating rate of 1.39 nm/min for 300 s. The resulting fibers were sputter coated and imaged using SEM. Scanning electron microscopy (SEM) was performed on a Thermo Fisher Scientific Apreo S. Fiber diameter and directionality were characterized using the measurement function and directionality plugin of NIH FIJI²⁹.

Substrate preparation and sterilization

Loctite silicone sealant was manually extruded through a plastic syringe to build walls around glass and fiber substrates and left to dry. The substrates were then affixed to a 4-well rectangular dish. Ethylene oxide (EtO) (Andersen Sterilizer, Haw River, NC) was used to sterilize the substrates via a 12 h sterilization cycle, followed by a 2 h aeration period. Sterilized substrates were then left for a minimum 72 h to allow residual EtO to diffuse out before migration experiments.

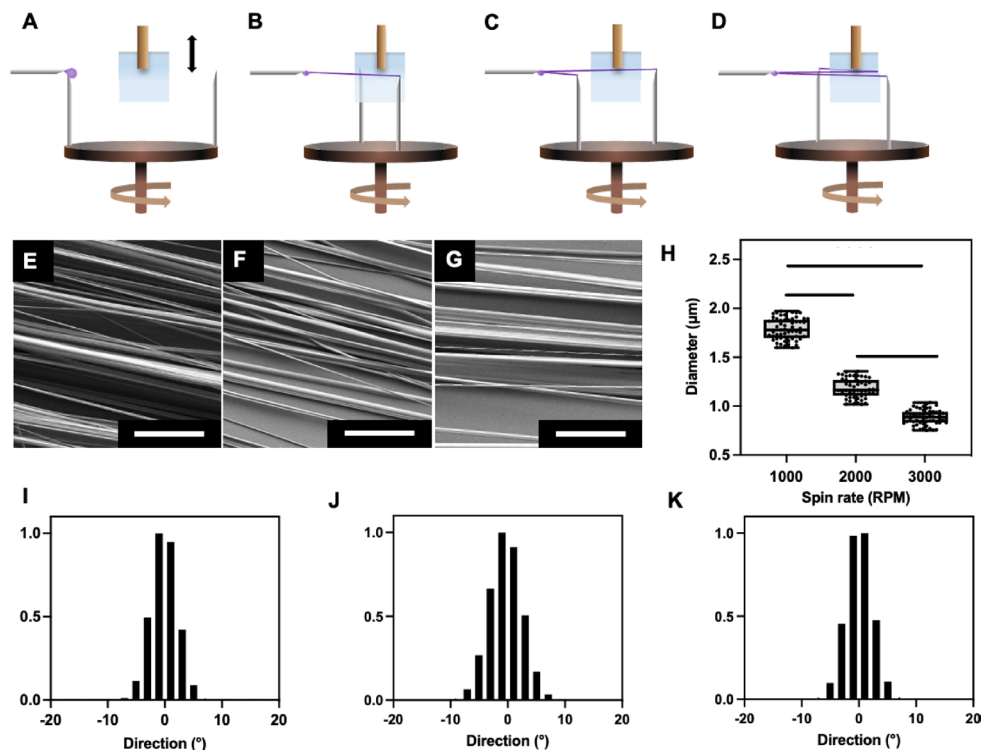


Fig. 1. Touch-spinning was used to fabricate highly aligned nanofiber scaffolds of different diameters. In touch-spinning, a platform spins at a defined and tunable rate, allowing for a needle/rod to (A) come into contact with a droplet of the polymer solution, (B, C) draw the droplet into a fiber mechanically, and (D) collect the fiber on a stationary center substrate (i.e., coverslip). Middle row: Representative SEM images of touch-spun, aligned nanofibers of diameters (E) 0.9 (F) 1.2 (G) 1.8 μm are shown. The scale bar represents 20 μm . (H) Fiber diameter as a function of spin rate. By increasing the spin rate of the rotating platform, fibers of smaller diameters were yielded. Significance was calculated using one-way ANOVA with Tukey as a post hoc test. Error bar: standard deviation. Bottom row: Fibers are highly aligned, with alignment distribution of (I) 0.9 (J) 1.2 (K) 1.8 μm fiber scaffolds. Three independent polymer solutions were used for fabrication and diameter measurement ($N=3$). At least 50 individual fibers (n) were measured (0.9 μm : $n=61$; 1.2 μm : $n=60$; 1.8 μm : $n=54$) for each population.

Isolation and maintenance of primary Schwann cells

Primary Schwann cells were isolated from female and male adult (3–5 months) Sprague Dawley rat sciatic nerves that were recently sacrificed from IACUC approved protocols. As no work was performed on live animals, this protocol did not need IACUC approval. Cells dissociated from the sciatic nerves were cultured using isolation media on flasks coated with poly-L-lysine ($1.5 \mu\text{g}/\text{cm}^2$)³⁰. All cells used in experiments were less than passage 5. The purity of the Schwann cells was verified via standard immunocytochemistry protocols. In short, samples were fixed with 4% (v/v) paraformaldehyde solution for 20 min, then permeabilized with 0.1% Triton X-100 for 20 min. Samples were subsequently incubated in 1 mg/mL sodium borohydride in PBS for 10 min (2x), washed with PBS, and blocked with 10% (w/v) BSA for 1 h at ambient temperature. Samples were then washed once with 1% (w/v) BSA and incubated in rabbit anti S-100 β primary antibody (1:250 in 1% (w/v) BSA) at 4 °C overnight. Cells were then incubated in Alexa Fluor™ 488 (AF488) goat anti-rabbit secondary antibody (1:100 in 1% (w/v) BSA) for 1 h at ambient temperature, washed with PBS, and labeled using Hoechst 33342.

Schwann cell purity quantification

The purity of Schwann cells at low ($\leq P2$) and high passages ($\geq P5$) was assessed by seeding and culturing Schwann cells at 5000 cell/ cm^2 in a 24-well tissue culture plate for 24 h. Schwann cells were then fixed and labeled as specified above. Three biological replicates were used ($N=3$) and three technical replicates were conducted for each biological replicate ($n=3$). Cells were observed and imaged using fluorescence microscopy and 7 images were taken of each substrate for a total of 21 images per biological replicate. Total cells that were S100 β^+ relative to all nuclei labeled were counted in each to quantify purity.

Cell culture and characterization

Primary female and male Schwann cells were cultured in proliferation media and seeded at a density of 2500 cells/ cm^2 in T25 flasks for general culturing. This seeding density was selected because previous research found cell–cell adhesions via cadherins were important in collective cellular locomotion³¹. N-cadherin is the primary receptor for intercellular adhesion between Schwann cells isolated from adult rat sciatic nerves, and the expression

of N-cadherin increases with cell numbers above 10.5×10^6 Schwann cells/cm²³². Therefore, culture was kept well below this threshold. Cell doubling time was calculated using a formula described previously³⁰. Viability assays were additionally conducted using the LIVE/DEAD™ Viability/Cytotoxicity Assay Kit for mammalian cells from Invitrogen following the manufacturer protocol at the 24 h timepoint (Figs. S11 and S12).

Cell culture media formulations

Isolation media was specifically designed to act as a fibroblast inhibitor and contained DMEM D-valine, forskolin (5 μM), FBS (10% vol/vol), N2 supplement (1% vol/vol), L-glutamine (1x), and BPE (14.2 μg/mL)³³. Proliferation media was identical to isolation media, except for the use of standard DMEM in place of DMEM D-valine. Seeding media contained DMEM and L-glutamine only. Migration media contained DMEM, FBS (10 vol/vol%), and L-glutamine (1x).

Live cell labeling

Media was removed from flasks and cells were washed with HBSS with Ca²⁺ and Mg²⁺. For each T25 flask, 2 mL of 250 nM CellTracker™ Deep Red Dye in HBSS with Ca²⁺ and Mg²⁺ was added. Each flask was then incubated for 30 min, followed by a wash with HBSS without Ca²⁺ and Mg²⁺.

Cell seeding

Control glass substrates were coated with laminin (mouse EHS, 2 μg/mL) on a shaker at 37 °C for 2 h and washed once with PBS. Fiber substrates were soaked in DMEM under reduced pressure for 30 min to enhance wetting for cell adhesion. Labeled cells were removed from flasks using trypsin (1x), counted, and resuspended in seeding media. All cells were seeded at a concentration of 10,000 cells/cm² for 4 h to allow for cell adhesion. The media was then removed and the cells were washed once with migration media. Each substrate then received an aliquot of migration media (1 mL) and was covered with Breath-Easy film to ensure minimal media evaporation over the duration of the experiment. Substrates were placed on the microscope to study cell migration.

Cell migration capture and tracking

Cell migration was recorded using the Zeiss Zen software by capturing an image every 15 min for 24 h on a Zeiss microscope equipped with a humidified and incubation module (5% CO₂, 37 °C). A manual tracking plugin in NIH FIJI was used to track the movement of individual cell centroids³⁴. For both female and male Schwann cells, at least 30 cells (n) were tracked per biological replicate. For each fiber diameter, three biological replicates (N=3) were studied, resulting in at least 100 cells used for data analysis. To be included in data analysis, each cell must have displaced at least 100 μm from the initial position at any point during the 24 h experiment. This criterion was imposed to ensure cells were migrating as opposed to exhibiting membrane extension. In addition, any cell that physically contacted other cells or obstacles during the time-lapse migration was manually excluded from data collection. Cells that exited the imaging boundaries were also excluded.

Morphological analysis

After 24 h cell migration study, samples were fixed with 4% paraformaldehyde in PBS, permeabilized with 0.1% Triton X-100 for 10 min, and quenched with 1 mg/mL sodium borohydride in PBS. Samples were blocked with 1 mg/mL BSA in PBS for 1 h at room temperature. To visualize actin filaments and nuclei, samples were then thrice washed with PBS for 5 min and incubated in a cocktail of AF488 phalloidin (1:200) and Hoechst 33342 (1:500) for 1 h at ambient temperature. Three biological replicates (N=3) and three technical replicates (n=3) were utilized. Cells were observed and imaged using fluorescence microscopy and 7 images were taken of each substrate for a total of 21 images per biological replicate. To quantify the influence of topography to actin alignment, images (n=21 per biological replicates) were analyzed using a previously described MATLAB method. This method utilized edge detection and statistical analysis to measure percent alignment $\pm 10^\circ$ of each cell relative to nanofiber orientation (100% indicates perfect alignment)^{25,35}. Morphologies of cell body and nucleus of each cell were manually traced in NIH FIJI. Average whole-cell aspect ratio ($\langle AR \rangle$), nuclear eccentricity ($\langle ER \rangle$) and angular positions of Schwann cells on each type of substrate were further calculated. Angular position of nuclei was subsequently plotted using a polar histogram program written in MATLAB³⁶.

Considerations for Schwann cell migration data inclusion

Criteria was embedded in the analysis of cell migration to remove cells that impacted each other during the 24 h tracking period. Previous studies have shown that cells seeded on nanofibers exhibit contact inhibition of locomotion after cell–cell contact, resulting in one of three responses: Type 1) both cells repolarizing and changing direction, Type 2) only one cell reversing, or Type 3) both cells exchanging positions³⁷. Although cells that experienced Type 3 interactions maintained their original migratory directions before contact with another cell, their fluorescence signals merged to be indistinguishable upon interaction and thus could not be tracked accurately. Therefore, in this study, cells that experienced interactions of Types 1–3 were manually removed from analysis to focus on cell–substrate correlation. After selection based on the criteria noted, at least 30 individual moving cells per biological replicate (N=3) were tracked and considered. As noted above, experiments were conducted in triplicate (n=3) to yield at least 100 individually migrating cells for analysis of cell–substrate interactions.

Data analysis for migration

Each analysis begins with the x,y positional data from cells, after exclusions as noted above, or with the mean squared displacement.

Mean squared displacement

The original position of each cell was defined as (0,0) and sequential positions (x, y) were recorded over time to plot migratory trajectories. Cell tracks were used to calculate mean-squared displacement (MSD) for overlapping intervals where x and y were the coordinates between time t and τ , the time lag, of each cell (Eq. 1).

$$MSD(\tau) = \langle [x(t - \tau) - x(t)]^2 + [y(t - \tau) - y(t)]^2 \rangle \quad (1)$$

$\tau = n \Delta t$ and $n = 1, 2, \dots, 96$, and Δt is the time step size (15 min). The ensemble average MSD and individual cell MSD were calculated using publicly available MATLAB code (*msd_analyzer*)³⁸, and further details for the calculations of these parameters can be found in the reference.

Velocity and instantaneous speed

On glass substrates, directions of x and y were selected, and noted as parallel and perpendicular to match those subscripts with the fiber substrates. The velocity in both x (\parallel) and y (\perp) were calculated at each interval for each cell. Velocity was then calculated as $\sqrt{v_x^2 + v_y^2}$. Instantaneous speed was then calculated as the absolute value of instantaneous velocity. On the fiber substrates, the direction of fiber alignment was defined as the x-axis (0°). Biased velocity $\langle \vec{V}_{\parallel} \rangle$ ($\mu\text{m}/\text{min}$) is the average velocity of an individual cell at each 15 min interval over 24 h along the x-axis. In contrast, $\langle \vec{V}_{\perp} \rangle$ ($\mu\text{m}/\text{min}$) is the average perpendicular velocity of an individual cell at each 15 min interval over 24 h. Speed in the x-axis is defined as the average absolute value of the velocity ($\langle |\vec{V}_{\parallel}| \rangle$) of an individual cell at each 15 min interval and is denoted as $\langle S_{\parallel} \rangle$ ($\mu\text{m}/\text{min}$). The average perpendicular speed is denoted as $\langle S_{\perp} \rangle$ ($\mu\text{m}/\text{min}$) and is defined similarly. The velocity vectors at each 15 min interval, denoted as $\langle \vec{V}_{\parallel} \rangle$ and $\langle \vec{V}_{\perp} \rangle$, were also calculated (Fig. S15D and E).

Persistence ratio

Persistence ratio (PR), known also as cell directionality ratio, was defined as the ratio of the displacement between start and end positions normalized to the total path length traveled. PR of both sexes on all substrates was calculated to determine how and if cell migration persisted³⁹.

Directional index

Directional index (DI) was defined as the ratio of the displacement in the positive x-direction between start and end positions normalized to the total path length traveled. If cells move in the negative x-direction, the DI would be negative. The average directional index ($\langle DI \rangle$) of both sexes on flat substrates was calculated to determine if cell migration had any directional persistence in the positive x direction⁴⁰.

Anomalous model

MSD curves were fitted and modeled to a logarithmic power law model, $\log \langle r^2(\tau) \rangle = \log(\Gamma \tau^{\alpha})$, then fit with a linear formula, $\Gamma + \alpha \log(\tau)$. The anomalous migration parameters were fit to the MSD curves for each cell using the first 25% of the overlapping time intervals (Fig. S19A). This percentage (25%) was utilized based on the publicly available code³⁸ and many other references using the first 25% of the data. Any individual MSD curve with a goodness of fit (R^2) (Fig. S19B), representing the quality of fit, of < 0.80 were excluded from the ensemble, as described previously³⁸. For the anomalous model, the slope α of the linear formula (α parameter) was extracted and provided information regarding cell diffusion in migration (Fig. S19C). Subdiffusive behavior is indicated by $0 < \alpha < 1$, meaning motion is constrained. Random migration is indicated by $\alpha = 1$, and superdiffusive behavior is indicated by $1 < \alpha < 2$ ⁴¹.

Persistent random walk model

The first 50% MSD curves, as the time lag becomes highly dependent on the earlier lags, of each individual cell on flat control substrates was fit to the following equation (Eq. 2) using a public MATLAB code⁴²:

$$MSD(\tau) = 2S^2P \left(\tau - P \left(1 - e^{-\tau/P} \right) \right) + 4\sigma^2 \quad (2)$$

using a non-linear least square method, with S as the cell speed ($\mu\text{m}/\text{min}$), P is persistence time (min), and $4\sigma^2$ is positional error for each cell^{41,42}. Goodness of fit (r^2) of each cell was determined to examine the fitting quality of the persistent random walk (PRW) model. The average S_{PRW} and P_{PRW} for each group is displayed in Fig. S15A and B, and the goodness of the fit, displayed as r^2 , was determined as > 0.9 for all cell paths (Fig. S15C).

The autocorrelation function of cell velocity and probability density function of cell displacements were calculated using the same code from Wu et al.⁴². Due to the probability density function of cell displacements showing a skewedness for the male cells (Fig. S16A), speed and persistence time were also fit to the anisotropic model even for the controls on glass substrates. Similar to the results from the PRW, S_p and S_{np} was higher for the female cells than their respective speeds for the male cells (Fig. S16C) and persistence time in the primary axis (P_p) was higher for the male cells than the female cells (Fig. S16B).

While the PRW model is constrained by a Gaussian distribution of cell positions, neither female (Fig. S19D) nor male (Fig. S19E) Schwann cells displayed a normal probability distribution for displacement. A stable distribution was a better fit to the probability density function (Fig. S19D–E). Using Matlab[®] to fit the Lévy stable distribution, parameters were determined to be: male— $\alpha = 1.453$, $\beta = 0.048$, $\gamma = 17.116$, $\delta = -$

0.193; female—alpha = 1.328, beta = - 0.025, gamma = 21.739, delta = 0.039. These parameters are within the ranges for a Lévy stable distribution where the stability parameter, alpha, is between 0 and 2, beta (the skewness parameter) is between - 1 and 1, gamma (the scale parameter) must be positive, and delta is the location parameter. Previous work has noted that Lévy walks are found in a variety of biological systems, including for predators and activated immune cells^{43,44}.

Anisotropic persistent random walk model

For both sexes, the goodness of fit for the velocity autocorrelations on flat substrates to a single-exponential decay were generally low ($r^2 < 0.5$), which rejected one of the key underlying assumptions of the PRW model⁴¹. Thus, an anisotropic persistent random walk (APRW) model was explored using a public MATLAB code⁴². Primary and non-primary migration directions of each cell were determined by the code. The first 50% primary and non-primary MSD of each cell was fitted to the APRW model using the following equations (Eqs. 3 and 4):

$$MSD_p(\tau) = S_p^2 P_p \left(\tau - P_p \left(1 - e^{-\tau/P_p} \right) \right) + 2\sigma_p^2 \quad (3)$$

$$MSD_{np}(\tau) = S_{np}^2 P_{np} \left(\tau - P_{np} \left(1 - e^{-\tau/P_{np}} \right) \right) + 2\sigma_{np}^2 \quad (4)$$

S_p and S_{np} are fit cell speeds ($\mu\text{m}/\text{min}$) and P_p and P_{np} are fit persistence times (min) in the primary and non-primary directions, respectively, and σ_p and σ_{np} are position errors.

Statistical analysis

All experiments were conducted in triplicate ($n = 3$) or as noted otherwise. At least 100 individual cells sourced from three different groups of animals ($N = 3$) of each sex were analyzed for each experiment. To compare differences between sexes on flat substrates, a two-tailed unpaired t-test was used for postnatal days (Fig. S9), doubling time (Fig. S10), morphology parameters (percentage of actin alignment (Fig. 2B), whole-cell AR (Fig. 2C), nuclear ER (Fig. 2D)), and motility parameters (α parameter (Fig. 3E), persistence ratio (Fig. 3F), speed (Fig. 4F), velocity (Fig. 4D), PRW and APRW-modeled speed and persistence time (Fig. S15 and S16)). To compare differences in motility and morphology parameters between sexes on fiber substrates, a two-way ANOVA test with Tukey as a post hoc test was used. Within each sex across fiber diameters, motility and morphology parameters were compared using one-way ANOVA test with Tukey as a post hoc test. To compare differences in MSD (Fig. 4B) and nuclear angle distribution (Fig. S14), 2-sample Kolmogorov–Smirnov test was used. All test methods were run with 95% confidence intervals ($p < 0.05$). To compare ensemble average MSD with time average MSD, ergodicity was calculated (Fig. S17). To compare methods of calculating an overall α , individual cell α and an α calculated by bootstrapping the ensemble average MSD were calculated for each sample and compared by unpaired t-tests (Fig. S18). Groups that were statistically different were marked with a solid line above the data. Groups that were not statistically different were left unmarked. Representative images of nuclei morphology and actin alignment of female and male Schwann cells were within the third quartile of quantification. All p values are reported within the Supporting Information (SI) (Tables S2 and S3).

Results and discussion

Synthesis and characterization of allyl-PCL

PCL is used widely in implantable medical devices, such as in vascular stents, films for tendon repair, and coatings for other degradable implants^{45–47}. However, the hydrophobicity of PCL generally leads to poor cell attachment and minimal surface wettability⁴⁸. Surface modification to introduce bioactive functionality or hydrophilic groups has often been necessary to enhance its integration and use^{28,48}. In the present study, allyl-PCL was synthesized via a ring opening copolymerization of ϵ -caprolactone (75 mol%) and 6-allyl- ϵ -caprolactone (A ϵ CL) (25 mol%). The presence of the allyl groups facilitate post-fabrication functionalization with cell adhesive peptides via thiol-ene click chemistry and the extent of peptide functionality can be tuned by stoichiometric control of monomer feed ratios during synthesis²⁸. The stoichiometry chosen afforded a high degree of functionality while maintaining the semi-crystalline nature of the PCL in order to form solid fibers that are stable at physiological temperatures.

Mg(BHT)₂(THF)₂ was chosen as the catalyst because its terminal oxidation product, magnesium oxide, is used as a food additive, and the chains maintain high end-group fidelity²⁷. Isopropanol was used as the initiator, but can be substituted with a number of functional alcohols to allow for additional biorthogonal functionalization opportunities to the end-groups²⁸. The copolymerization was complete in 5 h and yielded a high molecular mass ($M_w = 114$ kDa) and relatively narrow molecular mass distribution ($\mathcal{D}_M \sim 1.40$) copolymer (Fig. S6). The overall stoichiometry was confirmed by calculating the ratio between the integrations of the methine epsilon proton of A ϵ CL and the methylene epsilon protons of ϵ -caprolactone ($\delta = 4.9$ ppm and 4.1 ppm, respectively) (Fig. S5). Though the allyl-functionalities were not utilized in the present study, the introduction of such moieties was incorporated as proof-of-concept for future works that focus on fibers functionalized with bioactive peptides.

Touch-spun aligned nanofibers

PCL has been used widely in fibrous scaffolds for applications from drug delivery to tissue engineering^{49,50}. The majority of these works utilize electrospinning for scaffold fabrication^{23,50}. Production of aligned fibers via touch-spinning does not require the use of high-voltage electric fields to form liquid jets from a Taylor cone and instead relies on the mechanical drawing of fibers from concentrated polymer solutions (Fig. 1A–D)⁵¹. Touch-

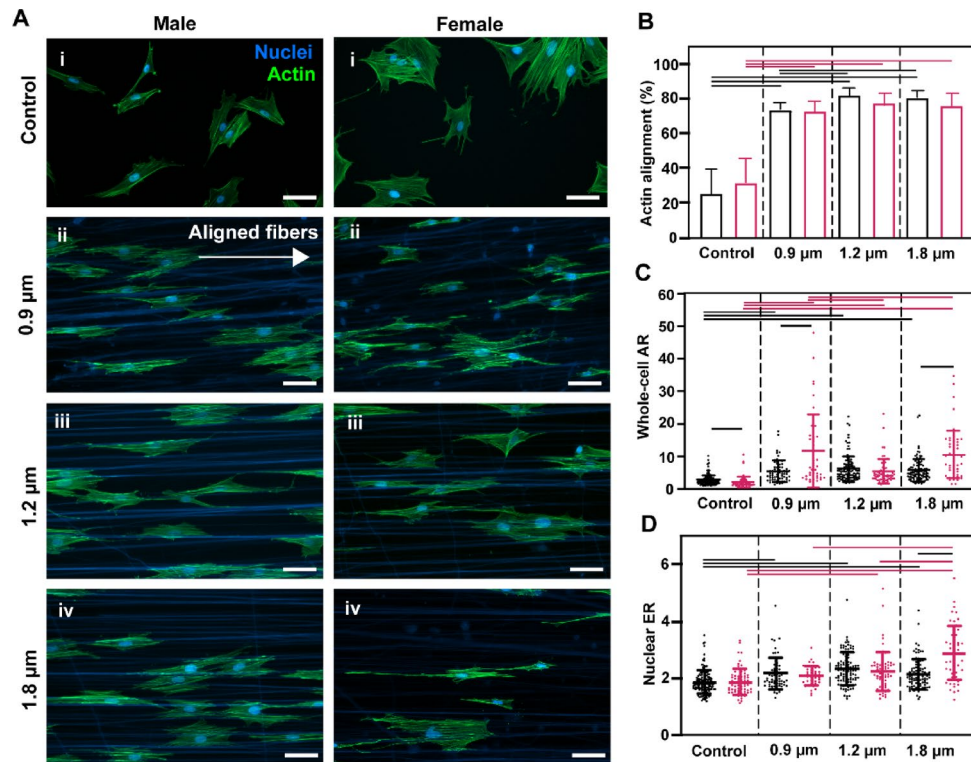


Fig. 2. Schwann cell morphology was elongated on nanofibers. **(A)** Representative images of aligned actin filaments of male (left) and female (right) Schwann cells on (i) controls (ii) 0.9 μm (iii) 1.2 μm (iv) 1.8 μm diameter fibers. The direction of aligned fibers is indicated by the white arrow along the horizontal axis. Actin filaments (green) were labeled using phalloidin-Alexa Fluor 488 and the cell nuclei (blue) were labeled using Hoechst 33342. Scale bar: 50 μm . Images are of the closest data point to the mean in the third quartile of the violin plots. 7 images were taken of each substrate for a total of 21 images per biological replicate. **(B)** Percentage of actin alignment was measured using a MATLAB edge detection program³⁵. No significant differences were found between female and male cells within any experimental condition. Values reported represent mean \pm standard deviation, where 100% indicates perfect alignment. **(C)** Whole-cell aspect ratio (AR) of individual female and male Schwann cells was measured. Whole-cell AR of male cells was statistically higher than female cells on flat substrates, while female cells are higher than males on 0.9 μm and 1.8 μm fibers. **(D)** Nuclear eccentricity ratio (ER) of individual female and male Schwann cells was separately examined. ER of female cells on 1.8 μm fibers was statistically higher than male cells. Three biological replicates were completed per sex ($N=3$), and greater than 40 individual cells (n) were measured (control: $n_{\text{male}}=144$, $n_{\text{female}}=68$; 0.9 μm : $n_{\text{male}}=66$, $n_{\text{female}}=40$; 1.2 μm : $n_{\text{male}}=103$, $n_{\text{female}}=63$; 1.8 μm : $n_{\text{male}}=101$, $n_{\text{female}}=52$). Statistical analyses were calculated using two-tailed unpaired t-test (control) and two-way ANOVA test with Tukey as a post hoc test (fiber). Error bar: standard deviation.

spun fibers exhibit increased Young's moduli, E , when compared to electrospun counterparts due to a higher degree of stretch-induced crystallinity⁵². Using touch-spinning, nanofibers of different diameters were obtained by varying the rotational speed. Using a constant input flow rate of 5 $\mu\text{L}/\text{min}$ (0.50 mg/mL polymer in CHCl_3) and varying speeds of 1000, 2000, and 3000 rotations per minute (RPM), nanofiber substrates with diameters ($0.88 \pm 0.07 \mu\text{m}$, $1.18 \pm 0.10 \mu\text{m}$, $1.78 \pm 0.11 \mu\text{m}$; referred as 0.9 μm , 1.2 μm and 1.8 μm fibers) were fabricated and confirmed by scanning electron microscopy (Fig. 1E–H). Angular distribution of fibers was measured and showed narrow ranges of -10° to 10° , confirming a high degree of alignment (Fig. 1I–K).

Characterization of animal age and Schwann cell purity

In addition to sexual dimorphism, other factors, such as age, correlate to functional and morphological differences within cells^{53,54}. Age of host has been known to influence neural cell function in mammalian animal models^{55–57}. For example, Schwann cells from 24-month old mice exhibited an impairment of functional recovery after nerve injury when compared to 2-month old mice; the performance of nerve graft implants was a function of age of the transplant rather than age of the host⁵⁸. Therefore, the ages of the animals used here were tracked and controlled. For each experiment, three experimental animal replicates were defined per sex, with each biological replicate including 4–6 sciatic nerves collected from 2–3 rats. No significant differences were found between average age of female (124 days; $n=3$) and male (143 days; $n=3$) rats used in the experiments (Fig. S9). In addition, the average doubling time of female ($51 \pm 14 \text{ h}$) and male Schwann cell groups ($53 \pm 16 \text{ h}$) at each passage were not statistically different (Fig. S10).

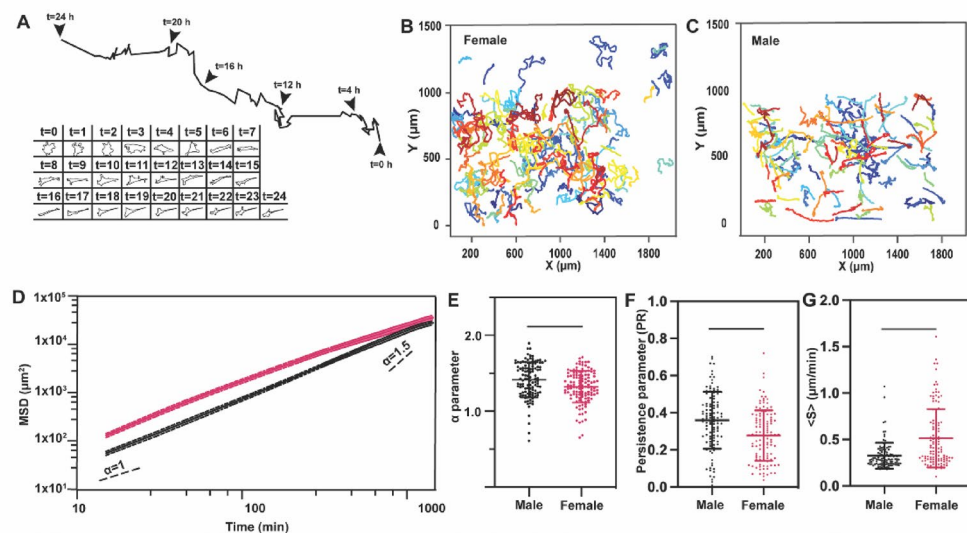


Fig. 3. Female and male Schwann cells possess inherent sex-based differences on flat laminin-coated substrates. (A) Sample cell path with cellular morphology at several times (t). Both path and cell shape are noted, with shapes shown from each hour of the capture. (B, C) Cell paths of female and male cells, respectively, are plotted over the course of the 24 h, with starting points centered at 0,0. (D) Ensemble average MSD curves on a log-log scale indicated significant differences in fit parameters each model. (E) According to the anomalous migration model, male cells exhibited a greater α parameter ($\alpha = 1.41 \pm 0.24$) than females ($\alpha = 1.32 \pm 0.21$), although both sexes were superdiffusive ($1 < \alpha < 2$). (F) In addition, male cells persisted in one direction longer than female cells as calculated by PR, and (G) female Schwann cells had higher average instantaneous speeds than male Schwann cells ($\langle S \rangle_{\text{female}} = 0.51 \pm 0.31 \mu\text{m/min}$; $\langle S \rangle_{\text{male}} = 0.33 \pm 0.14 \mu\text{m/min}$). Three biological replicates ($N = 3$) were completed per sex, where at least 100 individual cells were included ($n_{\text{male}} = 113$, $n_{\text{female}} = 121$). Statistical analyses for the α parameters and average speeds were calculated using two-tailed unpaired t-test. Error bar: standard deviation.

Fibroblasts and Schwann cells account for over 65% of the total cell population within peripheral nerves, making them the two most abundant cell types when isolated from animal hosts⁵⁹. However, proliferation rates of primary Schwann cells are relatively slow when compared to fibroblasts, meaning contamination by fibroblasts in Schwann cell culture can occur. D-valine-containing DMEM was used to selectively inhibit fibroblast proliferation; the expression of D-amino acid oxidase in Schwann cells allows for the conversion of D-valine to L-valine, an essential amino acid necessary for growth and survival³³. Fibroblasts do not have D-amino acid oxidase and cannot metabolize the isoform, resulting in the elimination of fibroblasts in the population due to essential amino acid depletion³³. To assess population purity, Schwann cells were labeled for S100 β and counted. Purity was determined as the number of S100 β ⁺ cells divided by the number of total cells. All female and male Schwann cell replicate groups demonstrated an average purity exceeding 97% at both low ($\leq P2$) and high ($\geq P5$) passages (Table S1), indicating little to no fibroblast contamination.

Effects of sex and fiber diameter on cell morphology

Surface topography impacts cell morphology and studies have shown that anisotropic nanofiber structures induce cellular morphological changes that control cell migration^{60,61}. To quantify effects of substrate topography on Schwann cell morphology, actin alignment, nucleus alignment, average whole-cell aspect ratio ($\langle AR \rangle$), and average nuclear eccentricity ratio ($\langle ER \rangle$) were used to describe cellular shape and polarization.

Cell orientation was examined by visualizing and quantifying F-actin filament and nucleus alignment to the nanofibers. As expected, only 25–30% of actin filaments on control surfaces were aligned at random for both female and male Schwann cells. When confined by fiber topography, cells were visibly aligned for both sexes in the direction of fibers (Fig. 2A). Actin alignment percentage increased to approximately 70–80% for both sexes on all fiber samples (Fig. 2B). No statistical difference between sexes were detected for actin alignment across fiber diameters. The angle of the nucleus with respect to the alignment of fibers was also examined (Figs. S13 and 14). Nuclei of both sexes were randomly distributed between -90° and 90° (0° = perfect alignment of the nucleus in one axis) on flat surfaces. On fiber samples, nuclear angle distribution was confined to a much narrower range of -10° to $+10^\circ$, where 0° was perfect alignment of the nucleus in fiber direction, demonstrating alignment was influenced by fiber orientation. These measurements indicated a significant effect on both cell and nucleus alignment due to the fibers, which agrees with previous research^{25,62}.

In addition to alignment with the nanofibers, overall Schwann cell shape was investigated at both the whole cell and nucleus levels. On glass surfaces, Schwann cells have typically exhibited a bipolar morphology, where the cell body is elongated in the direction of a polarized long axis⁶³. On glass surfaces used in this study, the $\langle AR \rangle$ of female and male Schwann cells was in agreement with other works, where $\langle AR \rangle$ was ≥ 2 (Fig. 2C)^{62,64}. When Schwann cells were seeded on fibers, $\langle AR \rangle$ increased for both sexes on all fiber diameters. However, female

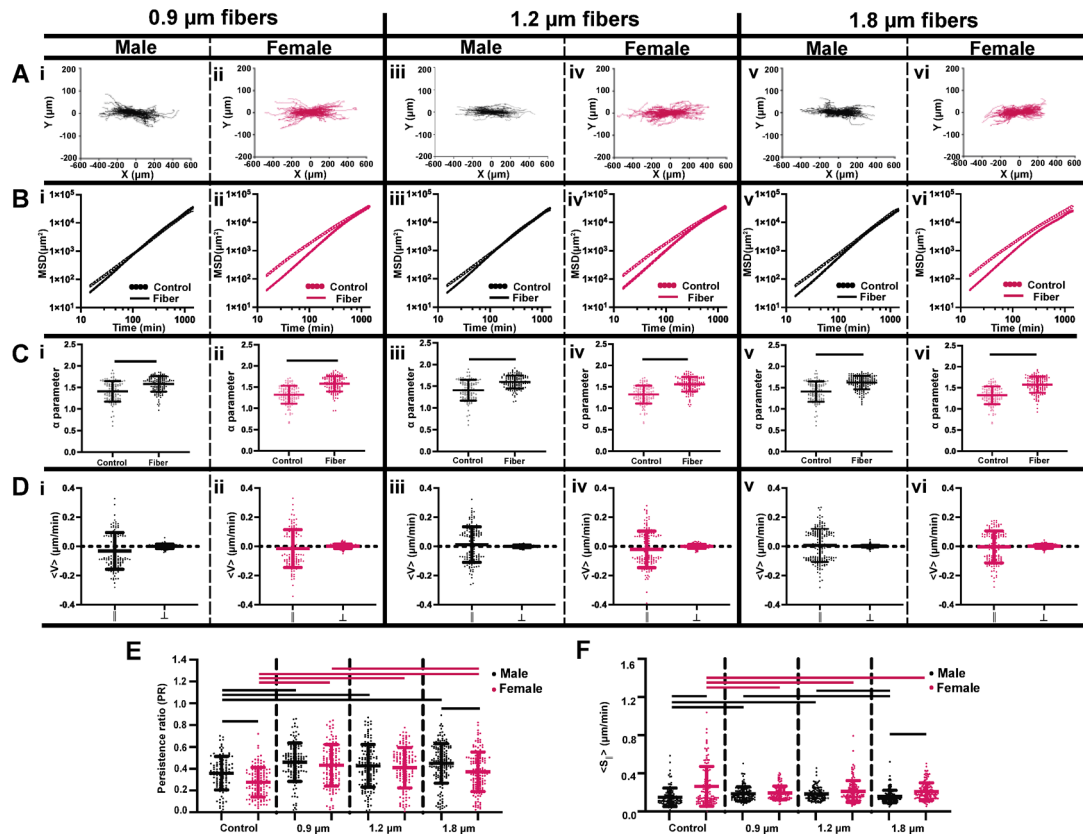


Fig. 4. Schwann cell migration on fibers reduced sex-based differences. (A) Cells paths indicate the influence of aligned fibers, with migration primarily along the x-axis of fiber alignment. Columns are separated by fiber diameter, with male (i, iii and v) in black and female (ii, iv and vi) in pink. (B) MSD was calculated and the MSD curve for 1.8 μm fibers was lower for females compared to other fibers and controls, but males showed no differences. Each graph has the MSD for the appropriate fiber group and its flat control. (C) The fit of a for anomalous migration was found to increase over controls but showed no differences between the sexes. The increase in α for fibers indicated further increased persistence. Within each sex, α parameters statistically increased on fibers compared to flat substrates. (D) The velocity vector indicated that the movement was primarily in the x-direction, as expected, with cells moving back and forth along the fiber, averaging to a 0 overall velocity. (E) The PR was again calculated for the fibers and while it increased from controls, minimal differences were found between the sexes except on 1.8 μm fibers, where male cells were more persistent than female cells. (F) The differences in speed (along fiber axis or x axis for controls) between sex was reduced with the addition of fibers at 0.9 μm , but the female cells showed increased speed with the larger fibers over male cells. Three biological replicates ($N = 3$) were completed per sex, where at least 100 individual cells were included (0.9 μm - $n_{\text{male}} = 124$, $n_{\text{female}} = 124$; 1.2 μm - $n_{\text{male}} = 138$, $n_{\text{female}} = 134$; 1.8 μm - $n_{\text{male}} = 169$, $n_{\text{female}} = 139$). Statistical analyses were calculated using two-tailed unpaired t-test (control) and two-way ANOVA test with Tukey as a post hoc test (fiber). Error bar: standard deviation.

Schwann cells had significantly higher $\langle AR \rangle$ than male Schwann cells on 0.9 μm ($p < 0.0001$) and 1.8 μm fibers (female - 0.9 μm : 11.95 ± 11.30 , 1.8 μm : 10.66 ± 7.31 ; male - 0.9 μm : 5.46 ± 3.28 , 1.8 μm : 5.76 ± 3.49) (Fig. 2C). Surprisingly, no differences were found between female and male cells on 1.2 μm fibers (female - 5.34 ± 3.89 ; male - 6.31 ± 4.03 ; $p = 0.979$). Thus, a diameter-dependent sex-based difference in cellular morphology was observed. Similar to whole-cell $\langle AR \rangle$, nuclear eccentricity ratio ($\langle ER \rangle$) of both sexes increased on nanofibers compared to controls (females - control: 1.85 ± 0.45 , 0.9 μm : 2.07 ± 0.35 , 1.2 μm : 2.25 ± 0.68 , 1.8 μm : 2.88 ± 0.95 ; males - control: 1.85 ± 0.41 , 0.9 μm : 2.16 ± 0.56 , 1.2 μm : 2.32 ± 0.57 , 1.8 μm : 2.13 ± 0.52) (Fig. 2D). On the largest fiber diameters (1.8 μm), female and male Schwann cells exhibited statistically different $\langle ER \rangle$ compared to each other ($p < 0.0001$). No differences in $\langle ER \rangle$ between sexes were observed on 0.9 and 1.2 μm fibers. While male Schwann cells did not exhibit diameter-dependent changes in $\langle ER \rangle$, female cells did show differences across fiber sizes, with higher $\langle ER \rangle$ on 1.8 μm fibers. These results agreed with previous work that indicated nanofibers modulate cellular shape in a diameter-dependent manner^{25,65}, with the additional finding of sex-based differences in both cellular and nucleus elongation on 1.8 μm fibers.

Innate sex-based migration differences

The deviations in the morphological responses suggested possible differences in cell migration between female and male cells⁶⁶. Female and male Schwann cells were first tracked in vitro on a flat, laminin-coated glass substrate

(Fig. 3A–C), determining x,y position every 15 min over 24 h. From the cell paths, mean-squared displacement (MSD) curves were used as a metric to quantify cell motility in time-lapse migration^{42,67}. From the MSD, the PRW model⁴² was fit for each cell on flat substrates, with results of $\langle S_{PRW} \rangle_{male} = 0.41 \pm 0.33 \mu\text{m}/\text{min}$ and $\langle S_{PRW} \rangle_{female} = 0.73 \pm 0.64 \mu\text{m}/\text{min}$ (Fig. S15A), and persistence times of $\langle P_{PRW} \rangle_{male} = 97.4 \pm 123.4 \text{ min}$ and $\langle P_{PRW} \rangle_{female} = 49.9 \pm 55.7 \text{ min}$ (Fig. S15B), with high average $r^2 \sim 0.90$ (Fig. S15C). In addition, the male cells had an elevated distribution along the 0–180° axis for the probability density distribution of angular displacements, indicating a preferred axis of migration (Fig. S16A)⁴². This result was not seen in female cells, which had an equal distribution of angular displacements.

The MSD versus time plots were transformed to a log–log scale (Fig. 3D) to assess anomalous migration parameters, where the slope of the curve (α parameter) gave information regarding randomness of migration, with Γ as the y-intercept (Fig. S19A). An α parameter of ~ 1 indicates random migration, while $1 < \alpha < 2$ indicates superdiffusive migration and $\alpha = 2$ indicates perfectly directed movement²⁵. The fit of the anomalous migration parameters was also excellent, with all included cells having an r^2 fit of > 0.91 (Fig. S19B). Both female and male cells on flat substrates had mean α parameters greater than 1, but male Schwann cells were observed to have a larger mean α parameter than female cells ($\alpha_{female} = 1.32 \pm 0.21$; $\alpha_{male} = 1.41 \pm 0.24$; $p = 0.0033$) (Fig. 3E). The α parameter provided a descriptive overall behavior of the migration and both sexes exhibited inherent superdiffusive behavior. Few tracked cells of either sex had an α below 1 (Fig. S19C). The goodness of fit for various models of migration has been explored for various types of cells, and most report similarly good fits as reported here on 2D flat substrates^{42,68}. However, because of timescales of experiments, it is difficult to fully evaluate models over long enough time periods to determine the best model⁶⁹. While 2D migration of Schwann cells on glass also fit a Lévy distribution (Fig. S19D–E), the amount of data being assessed, as well as the 24 h time frame of data collection, allow all models used to fit well.

With the α parameter indicating superdiffusive behavior, we investigated persistence from the velocity autocorrelation. The velocity autocorrelation in x and y were similar for female cells for the flat substrates, but not for male cells (Fig. S20A, B), and a time constant indicating persistence time was calculated as $1/\text{rate of exponential decay of the normalized velocity autocorrelation}$ ⁴². However, the fit of the velocity autocorrelation curve was generally low ($r^2 < 0.5$) by cell, indicating that the cells were not well represented by the PRW model⁴¹. To further investigate the persistence, therefore, PR was calculated by normalizing the absolute displacement from start to end points with the total path length traveled³⁹. Similar to the sex-based differences in the persistence time (P) via PRW model, PR was increased for male cells (Fig. 3F) over female cells. Motility characteristics of both superdiffusion and persistence indicated active migration, and have been correlated to metastasis⁴⁴ and effector T cells⁴³ as a search strategy to find targets. In this context, Schwann cell superdiffusive movement could be correlated with active repair processes induced by their culture and expansion. However, this activity does not explain the potential differences between the sexes.

The inherent deviations from a random walk ($\alpha \sim 1$) led us to further analyze speed (S) directly from the cell paths in addition to the model fits. Instantaneous cell speed was calculated using the individual cell paths at each point ($\Delta t = 15 \text{ min}$), along both dimensions of the flat plane. On flat substrates, sex-based differences were observed in overall average speed ($\langle S \rangle$), showing female Schwann cells migrating statistically faster than males ($\langle S \rangle_{female} = 0.51 \pm 0.31 \mu\text{m}/\text{min}$; $\langle S \rangle_{male} = 0.33 \pm 0.14 \mu\text{m}/\text{min}$) (Fig. 3G). To determine if cells had a bias in their directional movement, they were further characterized using directional velocity vectors (V_{\parallel} and V_{\perp}), and average directional index ($\langle DI \rangle$) which describes a cell's positive or negative displacement relative to its overall displacement⁴⁰. On flat surfaces, female and male Schwann cells exhibited an overall average near-zero $\langle \vec{V}_{\parallel} \rangle$, $\langle \vec{V}_{\perp} \rangle$, and $\langle DI \rangle$, describing an absence of biased migration (Figs. S15D, E and S20C).

Schwann cells exhibited innate migration differences between the sexes related to both MSD and speed, providing new information regarding peripheral nerve regeneration. First, while Schwann cells are steroidogenic and capable of neuroactive steroid synthesis, few studies have investigated sex-based differences of Schwann cells in vivo^{70,71} or in vitro^{72,73}. Therefore, the demonstration of inherent sex-based differences in Schwann cell migration is an important outcome. Generally, when reported, speeds for Schwann cell migration in vitro on flat substrates with peptides or proteins were similar to the speeds calculated here, but were either not identified by sex^{61,74} or the reports had female-only cells³⁰. In addition, many Schwann cell migration reports also used dorsal root ganglia as the cell source^{75,76}, limiting the ability of the cells to be tracked or quantified due to the multiple cell types in the ex vivo tissue. Our results both identify and quantify a difference between Schwann cell function that could result in differences in endogenous regeneration between sexes. Based on the differences we found in inherent control migration, fibers were introduced to characterize how topography influenced migration of female versus male cells.

Effects of sex and fiber diameter on cell migration

Because of their ability to direct and enhance neurite outgrowth along a single axis⁷⁷, aligned fiber scaffolds have been proposed for neural tissue engineering applications. As Schwann cell infiltration is integral to axonal regrowth, Schwann cell migration on aligned nanofiber substrates is important to understand during the device design process. Importantly, nanofibers have been found to provide topographical cues that impact cell migration²⁵. We investigated Schwann cell migration on aligned fiber scaffolds of three different fiber sizes ($0.88 \pm 0.07 \mu\text{m}$, $1.18 \pm 0.10 \mu\text{m}$, $1.78 \pm 0.11 \mu\text{m}$, referred to as $0.9 \mu\text{m}$, $1.2 \mu\text{m}$, and $1.8 \mu\text{m}$, respectively) to provide detailed analysis on sex-related cell responses as a function of fiber diameter. The diameters of the nanofibers used matched typical fibers found in the nerve in vivo, including individual nerve fibers, axons, myelin, and endogenous collagen fiber bundles in the endoneurium ($1\text{--}3 \mu\text{m}$ in diameter)^{78,79}, and thus, extend previous in vitro studies^{25,80}.

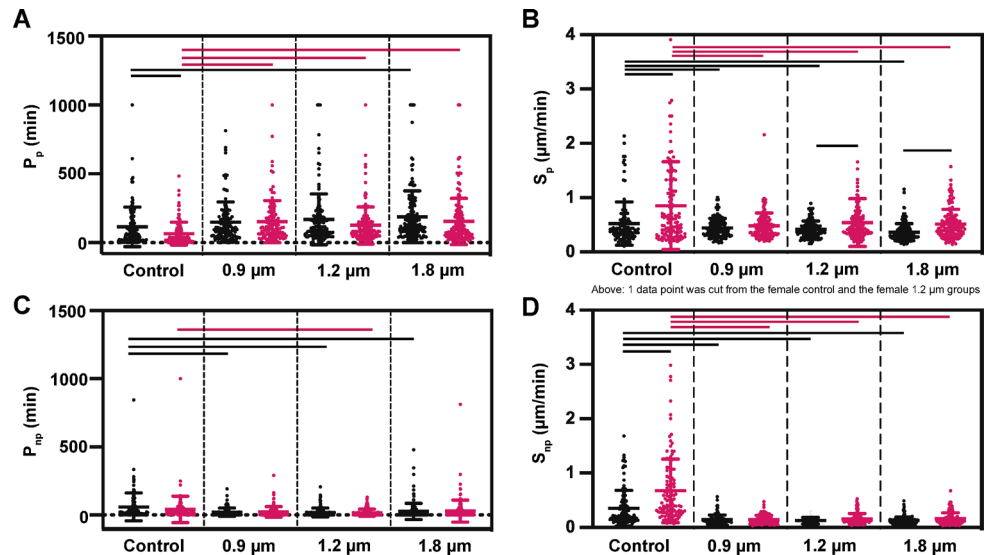


Fig. 5. APRW model fit to Schwann cell migration on aligned fibers. **(A)** The presence of fibers increased the persistence time of female cells along the fibers (primary direction, p) compared to controls, although it diminished the differences in persistence time seen between the sexes. Only the highest fiber diameters further increase the persistence time of male cells compared to controls. **(B)** The speed of both male and female cells on fibers (in the primary direction) is statistically decreased compared to sex-based controls, although the speed of female cells remains higher compared to male cells on the larger fibers. **(C and D)** Persistence time and speed fit for APRW model in the perpendicular direction (non-primary, np), with decreased persistence times and speed with the addition of fibers for both male and female cells. Three biological replicates ($N = 3$) were completed per sex, where at least 100 individual cells were included ($0.9 \mu\text{m} - n_{\text{male}} = 124, n_{\text{female}} = 124$; $1.2 \mu\text{m} - n_{\text{male}} = 138, n_{\text{female}} = 134$; $1.8 \mu\text{m} - n_{\text{male}} = 169, n_{\text{female}} = 139$). Statistical analyses were calculated using two-tailed unpaired t-test (control) and two-way ANOVA test with Tukey as a post hoc test (fibers). Error bar: standard deviation.

Similar to glass substrates, cell migration on fibers was measured via time lapse imaging of cells over a 24 h migration period. The cell paths indicated migration along the axis of the fibers (Fig. 4A). MSD trajectories of female and male Schwann cells on the three fiber sizes was statistically compared (Fig. 4B) to assess overall differences in migration. Compared to controls, female Schwann cell MSD showed no differences on $0.9 \mu\text{m}$ and $1.2 \mu\text{m}$ fibers but demonstrated a statistical decrease in MSD on $1.8 \mu\text{m}$ fibers; within fiber groups, female Schwann cells exhibited a decreased MSD with $1.8 \mu\text{m}$ fiber diameter. On the other hand, male Schwann cell MSD consistently showed no difference between control and all fiber sizes; in addition, male Schwann cells exhibited no differences in MSD between different diameters.

As aligned fibers provided an anisotropic substrate, both the anomalous migration and the APRW models were fit. With the anomalous migration model, both female and male cells showed an increase in α parameter on fibers compared to controls (female - $\alpha_{0.9 \mu\text{m}} = 1.58 \pm 0.18$, $\alpha_{1.2 \mu\text{m}} = 1.56 \pm 0.17$, $\alpha_{1.8 \mu\text{m}} = 1.57 \pm 0.19$; male - $\alpha_{0.9 \mu\text{m}} = 1.58 \pm 0.18$, $\alpha_{1.2 \mu\text{m}} = 1.60 \pm 0.15$, $\alpha_{1.8 \mu\text{m}} = 1.62 \pm 0.15$) (Fig. 4C). The APRW model showed in persistence time along the alignment axis with the addition of the fibers, but no longer between the sexes (Fig. 5A). Interestingly, only the female cells showed statistical increases in persistence time with the addition of fibers, while the males only showed persistence time differences between the control and the largest fiber size of $1.8 \mu\text{m}$. The fit of speed along the primary axis (S_p) was decreased within the female cells with the addition of the fibers, but differences were still noted between the female and male cells on the 1.2 and $1.8 \mu\text{m}$ fibers (Fig. 5B). Similarly, the non-primary axis (S_{np}) showed differences in speed, but were more limited in persistence (Fig. 5C, D). In summary, all fiber samples showed superdiffusive migration, with female cells increasing in persistence time with each increase in fiber size and male cells only increasing persistence time on the largest fiber diameters. The increases in α relative to controls were likely connected to contact guidance principles^{25,81} that have demonstrated increased persistence and/or speed. Some of the sex-based differences with speed remained with the introduction of fibers, although this response was diameter dependent.

To further investigate these differences, directional velocity, speeds, and PR were calculated from the cell paths. Mean velocity in the direction of fiber alignment was defined as $\langle \vec{V}_{\parallel} \rangle$, while the mean velocity perpendicular to the fibers was defined as $\langle \vec{V}_{\perp} \rangle$ at each 15 min interval. The range of \vec{V}_{\parallel} was approximately -0.4 to $0.4 \mu\text{m}/\text{min}$ for all substrates, making $\langle \vec{V}_{\parallel} \rangle$ approximately 0 because cells moved back and forth along the fiber axis (Fig. 4D). The range of \vec{V}_{\perp} for the fiber samples was -0.0001 to $0.0001 \mu\text{m}/\text{min}$, indicating little migration in the direction perpendicular to the fibers. The average speed in the direction of the fibers ($\langle S_{\parallel} \rangle$) and perpendicular to the fibers ($\langle S_{\perp} \rangle$) were investigated. On controls, $\langle S_{\parallel} \rangle$ and $\langle S_{\perp} \rangle$ were observed to be $\sim 0.20 \mu\text{m}/\text{min}$ for male cells, and $\sim 0.30 \mu\text{m}/\text{min}$ for female cells, indicating that cells moved with equal speed along both axes. However, on

fibers, $\langle S_{\perp} \rangle$ for both female and male Schwann cells decreased to less than 0.09 $\mu\text{m}/\text{min}$, while $\langle S_{\parallel} \rangle$ remained similar to controls. Both velocity and speed results showed that Schwann cells seeded on aligned fibers had minimal motion perpendicular to fiber alignment, a phenomenon explained as a result of contact guidance²⁵. Interestingly, the introduction of aligned fiber topographies generally increased $\langle S_{\parallel} \rangle$ of male Schwann cells, but left $\langle S_{\parallel} \rangle$ of female cells relatively unchanged. Male cells on flat surfaces exhibited an $\langle S_{\parallel} \rangle$ of $0.19 \pm 0.09 \mu\text{m}/\text{min}$, which increased to $0.23 \pm 0.07 \mu\text{m}/\text{min}$ on 1.2 μm fibers, while female cells on flat surfaces exhibited an $\langle S_{\parallel} \rangle$ of $0.31 \pm 0.21 \mu\text{m}/\text{min}$, which decreased to $\sim 0.25 \mu\text{m}/\text{min}$ on all fiber substrates (Fig. 4F). Previous work on female Schwann cells found increases in $\langle S_{\parallel} \rangle$ from 0.16 $\mu\text{m}/\text{min}$ (0.3 μm fiber diameter) to 0.28 $\mu\text{m}/\text{min}$ (0.9 μm fiber diameter)²⁵, and this study here extends that range further to 1.8 μm with no differences in $\langle S_{\parallel} \rangle$ indicating a plateau in the effect of diameter. For male Schwann cells, we found that 0.9 μm and 1.2 μm fibers supported the fastest speed, with the largest fibers having decreased $\langle S_{\parallel} \rangle$. Finally, an increase in PR for female cells eliminated the sex-based differences seen on flat substrates on both 0.9 μm and 1.2 μm fibers (Fig. 4E). Therefore, while the fibers overall increased PR relative to controls, the sex-based persistence differences were not evident on the smaller fibers.

Therefore, inherent persistence differences may allow male cells to adjust to contact guided migration by increasing their speed, while female cells increased their persistence, but not their speed. Untangling persistence from speed has been a long-lived problem relative to cell migration. Blocking cell–matrix adhesions was one of few conditions where speed and persistence were uncoupled, with reduced adhesions increasing cell speed⁸². The fibers in our study were not functionalized with specific adhesion molecules, potentially mimicking a reduction in cell–matrix interactions to uncouple the speed and persistence. A coupling between speed and persistence has been found to be due to actin flow speed⁸³, with the universal coupling framework has noted that faster cells are more persistent. Further work is necessary to determine the inherent differences between the sexes related to cell speed and persistence, as well as coupling between the two. Nonetheless, sex-based differences varied relative to fiber diameter and measurement type. As it relates to biomaterial design for nerve regeneration, 0.9 μm and 1.2 μm fiber will provide support for cells of both sexes, both in contact guidance cues but also for speed in migration.

Conclusion

A series of aligned fibers with well-defined diameters were fabricated in this study. The fibers were used to characterize sex-based responses (viability, morphology, migration) of female and male Schwann cells in response to culture on fibers of different diameters. Morphological analysis showed the shape and orientation of female and male Schwann cells on fiber substrates were functions of both sex and fiber diameter. On fibers, female Schwann cells exhibited greater whole-cell elongation than males on 0.9 and 1.8 μm fibers and greater nucleus elongation on 1.2 and 1.8 μm fibers. Innate sex-based differences in cell motility (MSD-fit models, α parameter, speed) were observed on flat surfaces. Promisingly for clinical applications, the impact of sex-based differences was reduced with the introduction of nanofiber scaffolds, although both speed and persistence were impacted. No sex-based differences were observed in α parameter on all fiber diameters, although the introduction of fibers increased α parameter of both sexes. Speed in the aligned axis for female Schwann cells was decreased on all fiber substrates, while male Schwann cells experienced an increase with fiber diameter. These results suggest that Schwann cell behavior is both sex and diameter-dependent when cultured on variable topographies. As quantified, relative speed and persistence differences between sexes contribute to the understanding of cell motility and contact guidance in artificial 2D microenvironments in vitro.

Data availability

Data is displayed within the manuscript or supplementary information files. We are happy to share the raw data upon request and adequate ability to send the image/video files. Please contact the corresponding authors.

Received: 24 October 2024; Accepted: 24 July 2025

Published online: 07 August 2025

References

- Dunford, A. et al. Tumor-suppressor genes that escape from X-inactivation contribute to cancer sex bias. *Nat. Genet.* **49**, 10–16. <https://doi.org/10.1038/ng.3726> (2017).
- Oliva, M. et al. The impact of sex on gene expression across human tissues. *Science* <https://doi.org/10.1126/science.aba3066> (2020).
- Gupta, S. et al. Sex differences in neutrophil biology modulate response to type I interferons and immunometabolism. *Proc. Natl. Acad. Sci.* **117**, 16481–16491. <https://doi.org/10.1073/pnas.2003603117> (2020).
- Baron-Cohen, S., Knickmeyer, R. C. & Belmonte, M. K. Sex Differences in the brain: Implications for explaining autism. *Science* **310**, 819–823. <https://doi.org/10.1126/science.1115455> (2005).
- Klein, S. L. & Flanagan, K. L. Sex differences in immune responses. *Nat. Rev. Immunol.* **16**, 626–638. <https://doi.org/10.1038/nri.2016.90> (2016).
- Rathore, S. S., Wang, Y. & Krumholz, H. M. Sex-based differences in the effect of digoxin for the treatment of heart failure. *N. Engl. J. Med.* **347**, 1403–1411. <https://doi.org/10.1056/NEJMoa021266> (2002).
- Engeland, C. G., Sabzehei, B. & Marucha, P. T. Sex hormones and mucosal wound healing. *Brain Behav. Immun.* **23**, 629–635. <https://doi.org/10.1016/j.bbi.2008.12.001> (2009).
- Rodríguez-Montes, L. et al. Sex-biased gene expression across mammalian organ development and evolution. *Science* <https://doi.org/10.1126/science.adf1046> (2023).
- Knewton, K. E., Ohl, N. R. & Robinson, J. L. Estrogen signaling dictates musculoskeletal stem cell behavior: Sex differences in tissue repair. *Tissue Eng. Part B Rev.* **28**, 789–812. <https://doi.org/10.1089/ten.TEB.2021.0094> (2022).
- Alkayed, N. J. et al. Gender-linked brain injury in experimental stroke. *Stroke* **29**, 159–166. <https://doi.org/10.1161/01.STR.29.1.159> (1998).

11. Groswasser, Z., Cohen, M. & Keren, O. Female TBI patients recover better than males. *Brain Inj.* **12**, 805–808. <https://doi.org/10.1080/026990598122197> (1998).
12. Pizzamiglio, L., Mammucari, A. & Razzano, C. Evidence for sex differences in brain organization in recovery in aphasia. *Brain Lang.* **25**, 213–223. [https://doi.org/10.1016/0093-934X\(85\)90081-1](https://doi.org/10.1016/0093-934X(85)90081-1) (1985).
13. Jang, E.-H. et al. Comparing axon regeneration in male and female mice after peripheral nerve injury. *J. Neurosci. Res.* **99**, 2874–2887. <https://doi.org/10.1002/jnr.24955> (2021).
14. Wood, K. et al. Sex differences in the effectiveness of treadmill training in enhancing axon regeneration in injured peripheral nerves. *Dev. Neurobiol.* **72**, 688–698. <https://doi.org/10.1002/dneu.20960> (2012).
15. Stenberg, L. & Dahlin, L. B. Gender differences in nerve regeneration after sciatic nerve injury and repair in healthy and in type 2 diabetic Goto-Kakizaki rats. *BMC Neurosci.* **15**, 107. <https://doi.org/10.1186/1471-2202-15-107> (2014).
16. Stephens, K. E. et al. Sex differences in gene regulation in the dorsal root ganglion after nerve injury. *BMC Genomics* **20**, 147. <https://doi.org/10.1186/s12864-019-5512-9> (2019).
17. Cinteza, D., Persinaru, I., Maciuceanu Zarnescu, B. M., Ionescu, D. & Lascar, I. Peripheral nerve regeneration - an appraisal of the current treatment options. *Maedica (Bucur)* **10**, 65–68 (2015).
18. Fadia, N. B. et al. Long-gap peripheral nerve repair through sustained release of a neurotrophic factor in nonhuman primates. *Sci. Transl. Med.* <https://doi.org/10.1126/scitranslmed.aav7753> (2020).
19. Grinsell, D. & Keating, C. P. Peripheral nerve reconstruction after injury: a review of clinical and experimental therapies. *Biomed Res Int* **2014**, 698256. <https://doi.org/10.1155/2014/698256> (2014).
20. Sivak, W. N., Bliley, J. M. & Marra, K. G. in *Axon Growth and Regeneration: Methods and Protocols* (ed Andrew J. Murray) 139–148 (Springer New York, 2014).
21. Crook, B. S., Cullen, M. M. & Pidgeon, T. S. The role of tissue engineering and three-dimensional-Filled conduits in bridging nerve gaps: A review of recent advancements. *J. Hand Surg. Global Online*. <https://doi.org/10.1016/j.jhsg.2024.01.024>.
22. BaoLin, G. & Ma, P. X. Synthetic biodegradable functional polymers for tissue engineering: a brief review. *Sci. China Chem.* **57**, 490–500. <https://doi.org/10.1007/s11426-014-5086-y> (2014).
23. Schnell, E. et al. Guidance of glial cell migration and axonal growth on electrospun nanofibers of poly-ε-caprolactone and a collagen/poly-ε-caprolactone blend. *Biomaterials* **28**, 3012–3025. <https://doi.org/10.1016/j.biomaterials.2007.03.009> (2007).
24. Clements, M. P. et al. The wound microenvironment reprograms Schwann cells to invasive mesenchymal-like cells to drive peripheral nerve regeneration. *Neuron* **96**, 98–114.e117. <https://doi.org/10.1016/j.neuron.2017.09.008> (2017).
25. Cavanaugh, M. et al. Influence of touch-spun nanofiber diameter on contact guidance during peripheral nerve repair. *Biomacromol* **23**, 2635–2646. <https://doi.org/10.1021/acs.biomac.2c00379> (2022).
26. Chew, S. Y., Mi, R., Hoke, A. & Leong, K. W. Aligned protein-polymer composite fibers enhance nerve regeneration: A potential tissue-engineering platform. *Adv. Funct. Mater.* **17**, 1288–1296. <https://doi.org/10.1002/adfm.200600441> (2007).
27. Wilson, J. A. et al. Magnesium catalyzed polymerization of end functionalized Poly(propylene maleate) and Poly(propylene fumarate) for 3D printing of bioactive scaffolds. *J. Am. Chem. Soc.* **140**, 277–284. <https://doi.org/10.1021/jacs.7b09978> (2018).
28. Silant'yeva, E. A., Willits, R. K. & Becker, M. L. Postfabrication Tethering of Molecular Gradients on Aligned Nanofibers of Functional Poly(ε-caprolactone)s. *Biomacromol* **20**, 4494–4501. <https://doi.org/10.1021/acs.biomac.9b01264> (2019).
29. Liu, Z. Q. Scale space approach to directional analysis of images. *Appl. Opt.* **30**, 1369–1373. <https://doi.org/10.1364/ao.30.001369> (1991).
30. Motta, C. M. M., Endres, K. J., Wesdemiotis, C., Willits, R. K. & Becker, M. L. Enhancing Schwann cell migration using concentration gradients of laminin-derived peptides. *Biomaterials* **218**, 119335. <https://doi.org/10.1016/j.biomaterials.2019.119335> (2019).
31. Venhuizen, J. H. & Zegers, M. M. Making heads or tails of it: Cell-cell adhesion in cellular and supracellular polarity in collective migration. *Cold Spring Harb. Perspect. Biol.* <https://doi.org/10.1101/cshperspect.a027854> (2017).
32. Wanner, I. B. et al. Role of N-cadherin in Schwann cell precursors of growing nerves. *Glia* **54**, 439–459. <https://doi.org/10.1002/glia.20390> (2006).
33. Kaewkhaw, R., Scutt, A. M. & Haycock, J. W. Integrated culture and purification of rat Schwann cells from freshly isolated adult tissue. *Nat. Protoc.* **7**, 1996–2004. <https://doi.org/10.1038/nprot.2012.118> (2012).
34. Schindelin, J. et al. Fiji: an open-source platform for biological-image analysis. *Nat. Methods* **9**, 676–682. <https://doi.org/10.1038/nmeth.2019> (2012).
35. Kemeny, S. F. & Clyne, A. M. A simplified implementation of edge detection in MATLAB is faster and more sensitive than fast fourier transform for actin fiber alignment quantification. *Microsc. Microanal.* **17**, 156–166. <https://doi.org/10.1017/s143192761100002x> (2011).
36. Zittrell, F. CircHist: Circular histogram in MATLAB. *Zenodo*. **10** (2019)
37. Singh, J., Pagulayan, A., Camley, B. A. & Nain, A. S. Rules of contact inhibition of locomotion for cells on suspended nanofibers. *Proc. Natl. Acad. Sci.* **118**, e2011815118. <https://doi.org/10.1073/pnas.2011815118> (2021).
38. Tarantino, N. et al. TNF and IL-1 exhibit distinct ubiquitin requirements for inducing NEMO-IKK supramolecular structures. *J. Cell Biol.* **204**, 231–245. <https://doi.org/10.1083/jcb.201307172> (2014).
39. Gorelik, R. & Gautreau, A. Quantitative and unbiased analysis of directional persistence in cell migration. *Nat. Protoc.* **9**, 1931–1943. <https://doi.org/10.1038/nprot.2014.131> (2014).
40. McCutcheon, M. Chemotaxis in leukocytes. *Physiol. Rev.* **26**, 319–336. <https://doi.org/10.1152/physrev.1946.26.3.319> (1946).
41. Wu, P.-H., Giri, A., Sun, S. X. & Wirtz, D. Three-dimensional cell migration does not follow a random walk. *Proc. Natl. Acad. Sci.* **111**, 3949–3954 (2014).
42. Wu, P. H., Giri, A. & Wirtz, D. Statistical analysis of cell migration in 3D using the anisotropic persistent random walk model. *Nat. Protoc.* **10**, 517–527. <https://doi.org/10.1038/nprot.2015.030> (2015).
43. Harris, T. H. et al. Generalized Levy walks and the role of chemokines in migration of effector CD8+ T cells. *Nature* **486**, 545–548. <https://doi.org/10.1038/nature11098> (2012).
44. Huda, S. et al. Levy-like movement patterns of metastatic cancer cells revealed in microfabricated systems and implicated in vivo. *Nat. Commun.* **9**, 4539. <https://doi.org/10.1038/s41467-018-06563-w> (2018).
45. Stewart, S. A. et al. Poly(caprolactone)-based coatings on 3D-printed biodegradable implants: A novel strategy to prolong delivery of hydrophilic drugs. *Mol. Pharm.* **17**, 3487–3500. <https://doi.org/10.1021/acs.molpharmaceut.0c00515> (2020).
46. Shen, Y. et al. Development of biodegradable polymeric stents for the treatment of cardiovascular diseases. *Biomolecules* <https://doi.org/10.3390/biom12091245> (2022).
47. Hu, J.-Z., Zhou, Y.-C., Huang, L.-H. & Lu, H.-B. Development of biodegradable polycaprolactone film as an internal fixation material to enhance tendon repair: an in vitro study. *BMC Musculoskelet. Disord.* **14**, 246. <https://doi.org/10.1186/1471-2474-14-246> (2013).
48. Yaseri, R., Fadaie, M., Mirzaei, E., Samadian, H. & Ebrahimezhad, A. Surface modification of polycaprolactone nanofibers through hydrolysis and aminolysis: a comparative study on structural characteristics, mechanical properties, and cellular performance. *Sci. Rep.* **13**, 9434. <https://doi.org/10.1038/s41598-023-36563-w> (2023).
49. Abdullah, T. et al. Sustainable drug release from polycaprolactone coated chitin-lignin gel fibrous scaffolds. *Sci. Rep.* **10**, 20428. <https://doi.org/10.1038/s41598-020-76971-w> (2020).
50. Sowmya, B., Hemavathi, A. B. & Panda, P. K. Poly (ε-caprolactone)-based electrospun nano-featured substrate for tissue engineering applications: A review. *Prog Biomater* **10**, 91–117. <https://doi.org/10.1007/s40204-021-00157-4> (2021).

51. Tokarev, A. et al. Touch- and brush-spinning of nanofibers. *Adv. Mater.* **27**, 6526–6532. <https://doi.org/10.1002/adma.201502768> (2015).
52. Lee, S.-J. et al. Touch-spun nanofibers for nerve regeneration. *ACS Appl. Mater. Interfaces*. **12**, 2067–2075. <https://doi.org/10.1021/acsami.9b18614> (2020).
53. Aufschneider, A. & Büttner, S. The vacuolar shapes of ageing: From function to morphology. *Biochimica et Biophysica Acta (BBA) – Mol. Cell Res.* **1866**, 957–970. <https://doi.org/10.1016/j.bbamcr.2019.02.011> (2019).
54. Guo, J. et al. Aging and aging-related diseases: from molecular mechanisms to interventions and treatments. *Signal Transduct. Target. Ther.* **7**, 391. <https://doi.org/10.1038/s41392-022-01251-0> (2022).
55. Scheib, J. & Höke, A. Impaired regeneration in aged nerves: Clearing out the old to make way for the new. *Exp. Neurol.* **284**, 79–83. <https://doi.org/10.1016/j.expneurol.2016.07.010> (2016).
56. Painter, M. W. Aging Schwann cells: mechanisms, implications, future directions. *Curr. Opin. Neurobiol.* **47**, 203–208. <https://doi.org/10.1016/j.conb.2017.10.022> (2017).
57. Pestronk, A., Schmidt, R. E., Bucelli, R. & Sim, J. Schwann cells and myelin in human peripheral nerve: Major protein components vary with age, axon size and pathology. *Neuropathol Appl. Neurobiol.* **49**, e12898. <https://doi.org/10.1111/nan.12898> (2023).
58. Painter, M. W. et al. Diminished Schwann cell repair responses underlie age-associated impaired axonal regeneration. *Neuron* **83**, 331–343. <https://doi.org/10.1016/j.neuron.2014.06.016> (2014).
59. Wolbert, J. et al. Redefining the heterogeneity of peripheral nerve cells in health and autoimmunity. *Proc. Natl. Acad. Sci.* **117**, 9466–9476. <https://doi.org/10.1073/pnas.1912139117> (2020).
60. Kievit, F. M. et al. Aligned chitosan-polycaprolactone polyblend nanofibers promote the migration of glioblastoma cells. *Adv. Healthcare Mater.* **2**, 1651–1659. <https://doi.org/10.1002/adhm.201300092> (2013).
61. Mitchell, J. A. & Hoffman-Kim, D. Cellular scale anisotropic topography guides Schwann cell motility. *PLoS ONE* **6**, e24316. <https://doi.org/10.1371/journal.pone.0024316> (2011).
62. Zheng, J. et al. Enhanced Schwann cell attachment and alignment using one-pot “dual click” GRGDS and YIGSR derivatized nanofibers. *Biomacromol* **16**, 357–363. <https://doi.org/10.1021/bm501552t> (2015).
63. Wang, Y., Teng, H. L. & Huang, Z. H. Intrinsic migratory properties of cultured Schwann cells based on single-cell migration assay. *PLoS ONE* **7**, e1824. <https://doi.org/10.1371/journal.pone.0051824> (2012).
64. Tonazzini, I., Jacchetti, E., Meucci, S., Beltram, F. & Cecchini, M. Schwann cell contact guidance versus boundary interaction in functional wound healing along nano and microstructured membranes. *Adv. Healthcare Mater.* **4**, 1849–1860. <https://doi.org/10.1002/adhm.201500268> (2015).
65. Refaai, F. M., Chen, X. & Pang, S. W. Effects of topographical guidance cues on osteoblast cell migration. *Sci. Rep.* **10**, 20003. <https://doi.org/10.1038/s41598-020-77103-0> (2020).
66. Liu, Y. et al. Morphological entropy encodes cellular migration strategies on multiple length scales. *NPJ. Syst. Biol. Appl.* **10**, 26. <https://doi.org/10.1038/s41540-024-00353-5> (2024).
67. Loosley, A. J., O'Brien, X. M., Reichner, J. S. & Tang, J. X. Describing directional cell migration with a characteristic directionality time. *PLoS ONE* **10**, e0127425. <https://doi.org/10.1371/journal.pone.0127425> (2015).
68. Luzhansky, I. D. et al. Anomalous diffusing and persistently migrating cells in 2D and 3D culture environments. *APL Bioeng.* **2**, 026112. <https://doi.org/10.1063/1.5019196> (2018).
69. Viswanathan, G. M., Raposo, E. P., Bartumeus, F., Catalan, J. & da Luz, M. G. Necessary criterion for distinguishing true superdiffusion from correlated random walk processes. *Phys. Rev. E Stat. Nonlin. Soft Matter. Phys.* **72**, 011111. <https://doi.org/10.1103/PhysRevE.72.011111> (2005).
70. Kovacic, U., Zele, T., Osredkar, J., Sketelj, J. & Bajrovic, F. F. Sex-related differences in the regeneration of sensory axons and recovery of nociception after peripheral nerve crush in the rat. *Exp. Neurol.* **189**, 94–104. <https://doi.org/10.1016/j.expneurol.2004.05.015> (2004).
71. Koenig, H. L. et al. Progesterone synthesis and myelin formation by Schwann cells. *Science* **268**, 1500–1503. <https://doi.org/10.1126/science.7770777> (1995).
72. Svenningsen, Å. F. & Kanje, M. Estrogen and progesterone stimulate Schwann cell proliferation in a sex- and age-dependent manner. *J. Neurosci. Res.* **57**, 124–130. [https://doi.org/10.1002/\(sici\)1097-4547\(19990701\)57:1%3c124::Aid-jnr13%3e3.0.Co;2-p](https://doi.org/10.1002/(sici)1097-4547(19990701)57:1%3c124::Aid-jnr13%3e3.0.Co;2-p) (1999).
73. Magnaghi, V. et al. Sex-dimorphic effects of progesterone and its reduced metabolites on gene expression of myelin proteins by rat Schwann cells. *J. Peripher. Nerv. Syst.* **11**, 111–118. <https://doi.org/10.1111/j.1085-9489.2006.00075.x> (2006).
74. Ahmed, Z. & Brown, R. A. Adhesion, alignment, and migration of cultured Schwann cells on ultrathin fibronectin fibres. *Cell Motil. Cytoskeleton*. **42**, 331–343. [https://doi.org/10.1002/\(sici\)1097-0169\(1999\)42:4%3c331::Aid-cm6%3e3.0.Co;2-7](https://doi.org/10.1002/(sici)1097-0169(1999)42:4%3c331::Aid-cm6%3e3.0.Co;2-7) (1999).
75. Wang, H. B., Mullins, M. E., Cregg, J. M., McCarthy, C. W. & Gilbert, R. J. Varying the diameter of aligned electrospun fibers alters neurite outgrowth and Schwann cell migration. *Acta Biomater.* **6**, 2970–2978. <https://doi.org/10.1016/j.actbio.2010.02.020> (2010).
76. Chen, S. et al. Promoting neurite growth and schwann cell migration by the harnessing decellularized nerve matrix onto Nanofibrous Guidance. *ACS Appl. Mater. Interfaces* **11**, 17167–17176. <https://doi.org/10.1021/acsami.9b01066> (2019).
77. Xie, J., MacEwan, M. R., Schwartz, A. G. & Xia, Y. Electrospun nanofibers for neural tissue engineering. *Nanoscale* **2**, 35–44 (2010).
78. Ikeda, M. & Oka, Y. The relationship between nerve conduction velocity and fiber morphology during peripheral nerve regeneration. *Brain Behav* **2**, 382–390. <https://doi.org/10.1002/brb3.61> (2012).
79. Jain, D., Mattiassi, S., Goh, E. L. & Yim, E. K. F. Extracellular matrix and biomimetic engineering microenvironment for neuronal differentiation. *Neural Regen Res.* **15**, 573–585. <https://doi.org/10.4103/1673-5374.266907> (2020).
80. Yang, F., Murugan, R., Wang, S. & Ramakrishna, S. Electrospinning of nano/micro scale poly(l-lactic acid) aligned fibers and their potential in neural tissue engineering. *Biomaterials* **26**, 2603–2610. <https://doi.org/10.1016/j.biomaterials.2004.06.051> (2005).
81. Ray, A. et al. Anisotropic forces from spatially constrained focal adhesions mediate contact guidance directed cell migration. *Nat. Commun.* **8**, 14923. <https://doi.org/10.1038/ncomms14923> (2017).
82. Leineweber, W. D. & Fraley, S. I. Adhesion tunes speed and persistence by coordinating protrusions and extracellular matrix remodeling. *Dev Cell* <https://doi.org/10.1016/j.devcel.2023.05.013> (2023).
83. Maiuri, P. et al. Actin flows mediate a universal coupling between cell speed and cell persistence. *Cell* **161**, 374–386. <https://doi.org/10.1016/j.cell.2015.01.056> (2015).

Acknowledgements

The authors are grateful for financial support from the National Institutes of Health (NINDS 1R01-NS124889-01A1). Additionally, this work was performed in part at the Duke University Shared Materials Instrumentation Facility (SMIF), a member of the North Carolina Research Triangle Nanotechnology Network (RTNN), which is supported by the National Science Foundation (award number ECCS-2025064) as part of the National Nanotechnology Coordinated Infrastructure (NNCI).

Author contributions

MLB and RKW conceived of and planned the work. YMC carried out the synthesis, characterization, and fabri-

cation of the polymer nanofibers used in this work, with assistance from NGJ. YH carried out the Schwann cell migration studies, MATLAB analysis, and statistical analysis. Miscellaneous cell studies (live/dead, purity, etc.) and data processing were shared by YMC and YH. The manuscript was written and prepared by YMC and YH, with the support of NGJ, MLB, and RKW.

Declarations

Competing interests

The authors declare no competing interests.

Additional information

Supplementary Information The online version contains supplementary material available at <https://doi.org/10.1038/s41598-025-13450-0>.

Correspondence and requests for materials should be addressed to M.L.B. or R.K.W.

Reprints and permissions information is available at www.nature.com/reprints.

Publisher's note Springer Nature remains neutral with regard to jurisdictional claims in published maps and institutional affiliations.

Open Access This article is licensed under a Creative Commons Attribution-NonCommercial-NoDerivatives 4.0 International License, which permits any non-commercial use, sharing, distribution and reproduction in any medium or format, as long as you give appropriate credit to the original author(s) and the source, provide a link to the Creative Commons licence, and indicate if you modified the licensed material. You do not have permission under this licence to share adapted material derived from this article or parts of it. The images or other third party material in this article are included in the article's Creative Commons licence, unless indicated otherwise in a credit line to the material. If material is not included in the article's Creative Commons licence and your intended use is not permitted by statutory regulation or exceeds the permitted use, you will need to obtain permission directly from the copyright holder. To view a copy of this licence, visit <http://creativecommons.org/licenses/by-nc-nd/4.0/>.

© The Author(s) 2025